APPLIED SCIENCES AND ENGINEERING

Laser writing of nitrogen-doped silicon carbide for biological modulation

Vishnu Nair[1,2]*, Jaeseok Yi[2]*, Dieter Isheim[3], Menahem Rotenberg[2], Lingyuan Meng[4], Fengyuan Shi[5], Xinqi Chen[6], Xiang Gao[2], Aleksander Prominski[1,2], Yuanwen Jiang[1,2], Jiping Yue[7], Charles T. Gallagher[8], David N. Seidman[3], Bozhi Tian[1,2,9]†

Conducting or semiconducting materials embedded in insulating polymeric substrates can be useful in biointerface applications; however, attainment of this composite configuration by direct chemical processes is challenging. Laser-assisted synthesis has evolved as a fast and inexpensive technique to prepare various materials, but its utility in the construction of biophysical tools or biomedical devices is less explored. Here, we use laser writing to convert portions of polydimethylsiloxane (PDMS) into nitrogen-doped cubic silicon carbide (3C-SiC). The dense 3C-SiC surface layer is connected to the PDMS matrix via a spongy graphite layer, facilitating electrochemical and photoelectrochemical activity. We demonstrate the fabrication of arbitrary two-dimensional (2D) SiC-based patterns in PDMS and freestanding 3D constructs. To establish the functionality of the laser-produced composite, we apply it as flexible electrodes for pacing isolated hearts and as photoelectrodes for local peroxide delivery to smooth muscle sheets.

INTRODUCTION

Laser-assisted processes are used in material synthesis because of their ease of use, low cost, and unique capacity to generate complex phases (*1*–*3*). Laser-produced composites can potentially expand the available design principles for materials and devices aimed at biological sensing and modulation (*4*). Recently, graphene/graphite-based conducting materials produced by laser writing were used for electrochemical sensing of metabolites in sweat (*5*, *6*), and further research efforts toward laser-assisted synthesis of conductors for biosensing are anticipated. In the current study, we focus on the laser-assisted production of semiconductors from elastomer substrates for biomodulation. For this purpose, we search for a material platform that will allow for the electronic, electrochemical, photoelectrochemical, and photothermal modulation of multiscale biological components, an area in which silicon (Si) has held prominence. The drawbacks of Si, however, include its degradation under physiological conditions and its limited electrochemical properties (*7*, *8*). Moreover, in comparison to semiconductor-based information processing systems, materials and devices used for bioelectronics or biomaterials must prioritize operational flexibility over structural precision. Hence, there is a demand in biointerface research to use methods such as laser writing or nozzle-based printing for the production of cheap and user-defined materials or devices (*9*, *10*).

Silicon carbide (SiC), in addition to its use as a common abrasive, is of importance to the semiconductor industry. Although SiC displays superb stability under physiological conditions, its utility in biological modulation from an optoelectronic or electronic perspective is underexplored. SiC synthesis methods range from conventional high-temperature inorganic methods, such as the Acheson process, to those that rely on organic precursors such as polysiloxanes (*11*–*15*). SiC is also known to form a plethora of polytypes, such as hexagonal 6H, cubic 3C, and rhombohedral 15R. The cubic 3C polytype, in particular, displays high electron mobility, thermal conductivity, and saturation drift velocity (*16*). However, the synthesis of 3C-SiC typically requires stringent growth conditions (*16*–*18*). Therefore, extension of 3C-SiC to applications such as bioelectronics necessitates exploration of new synthesis methods.

In this work, we demonstrate two-dimensional (2D) and 3D laser patterning of 3C-SiC using polydimethylsiloxane (PDMS) as a precursor. Laser ablation creates a dense SiC layer, which is connected to the insulating PDMS matrix by a loose graphite network (Fig. 1A). By controlling lasing conditions such as power and scan speed, we produce composites with surface, trench, and cut-through geometries (Fig. 1A). The laser-assisted process incorporates nitrogen as an n-type dopant in SiC. Together with the graphite network, the SiC in the flexible composite shows pseudocapacitive electrochemical behavior and photoelectrochemical activity. Surface functionalization of SiC with manganese dioxide (MnO_2 or MnO_x) further enhances the photoelectrochemical activity of the composite. Last, we use these SiC-based devices to modulate activity in isolated hearts (Fig. 1B) and cultured cells (Fig. 1C). Our work suggests that laser writing can efficiently produce flexible and multifunctional semiconductor/elastomer composites for biointerface studies.

RESULTS AND DISCUSSION

Synthesis and structural characteristics of SiC

We prepared a pure PDMS slab using a standard protocol and placed it on a commercial laser cutter platform. Using the control software and the 10.6-μm CO_2 laser, we ablated the PDMS in various patterns. During the ablation, the substrate was held under a nitrogen-rich atmosphere using the built-in nitrogen purging system. In addition to partially removing the PDMS, the lasing converted part of the remaining PDMS to a yellow-colored solid (fig. S1, F and G) and a

[1]Department of Chemistry, University of Chicago, Chicago, IL 60637, USA. [2]James Franck Institute, University of Chicago, Chicago, IL 60637, USA. [3]Northwestern University Center for Atom-Probe Tomography, Evanston, IL 60208, USA. [4]Pritzker School of Molecular Engineering, University of Chicago, Chicago, IL 60637, USA. [5]Electron Microscopy Core, University of Illinois Chicago, Chicago, IL 60607, USA. [6]Keck Interdisciplinary Surface Science Center, Northwestern University, Evanston, IL 60208, USA. [7]Ben May Department for Cancer Research, University of Chicago, Chicago, IL 60637, USA. [8]Department of Physics, University of Chicago, Chicago, IL 60637, USA. [9]Institute for Biophysical Dynamics, University of Chicago, Chicago, IL 60637, USA.
*These authors contributed equally to this work.
†Corresponding author. Email: btian@uchicago.edu

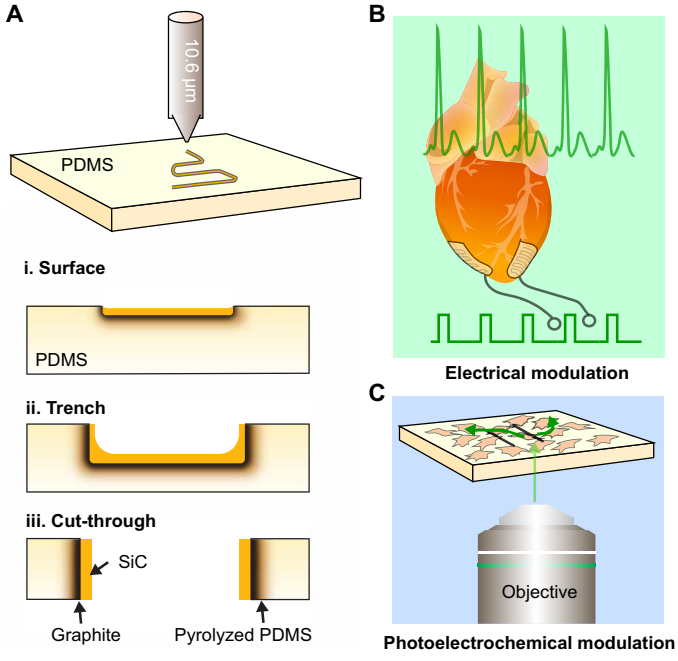

Fig. 1. Schematic illustrations of the laser writing process and its applications. (**A**) CO_2 laser writing a pattern on a PDMS substrate wherein the pattern can be (i) on the surface, (ii) a trench, or (iii) a cut-through leading to the formation of two distinct pieces. Architectures (i) to (iii) arise as a function of the laser power and writing speed. A graphite layer forms beneath the SiC because of the nature of the ablation process. (**B**) Laser-written electrodes are flexible electrodes that can integrate with a heart and stimulate it with electrical impulses leading to its pacing. (**C**) Laser-written circuits can be used for photoelectrochemical modulation of interconnected cellular ensembles.

thin, dark layer that connected the yellow solid to the PDMS matrix (Fig. 1A).

For structural analysis, the converted layers were removed from the PDMS matrix and microtomed. These sections were then characterized using high-angle annular dark-field scanning transmission electron microscopy (HAADF-STEM), TEM, and selected-area electron diffraction (SAED). STEM revealed an interface between a densely packed solid layer and a spongy network (Fig. 2A, left). High-resolution STEM images of portions of the spongy network showed layered lattices characteristic of graphite (Fig. 2A, middle and right). Bright-field TEM (Fig. 2B) of the densely packed region showed well-faceted crystals. SAED (Fig. 2C) and STEM (Fig. 2D) indicated that the dense solid contains 3C-SiC; this was supported by images recorded from the [011] zone of 3C-SiC (Fig. 2, B and C). As electron microscopy only identifies local information, we next used wide-angle x-ray scattering (WAXS) to characterize the crystal composition in well-ground composites. The WAXS pattern (Fig. 2E) showed peaks that were indexed to 3C-SiC, along with minor stacking faults (*19*) and a weak graphite (002) peak. These results confirmed that we had synthesized 3C-SiC connected to PDMS by a spongy graphite network. We attribute the difference in chemical conversion (i.e., 3C-SiC and graphite) to the existence of thermal gradients in the sample. During the ablation, a high temperature is expected in the direct laser spot, promoting conversion of PDMS to SiC. A lower temperature in the surrounding leads to carbonization and formation of a graphite layer (Figs. 1A and 2A). This one-step process and the intrinsic temperature gradient allow for in situ formation of a semiconductor-conductor junction, a configuration necessary for many electrochemical and photoelectrochemical devices (*20*).

To further analyze the chemical composition of the crystals with subnanometer resolution, we performed atom probe tomography (APT) on 3C-SiC (Fig. 2, F and G, and fig. S1). The 3D reconstructed APT image (Fig. 2F) and mass spectrometric analysis (Fig. 2G) revealed the presence of nitrogen (green spheres in Fig. 2F and green-labeled peaks in Fig. 2G); its association with silicon and carbon atoms in the 3C-SiC sample confirmed the n-type doping. Further concentration analysis of nitrogen showed a constant average nitrogen doping of ~215 parts per million in 3C-SiC (fig. S1F). The observed nitrogen doping is likely due to the high temperature of the laser ablation reaction that facilitates doping from the nitrogen-rich atmosphere (*21*).

2D and 3D printing

Utilization of a commercial laser cutter enabled us to control the printing resolution by adjusting laser power and scan speed. First, we studied 3C-SiC crystal formation and its grain size across a broad range of printing parameters (fig. S2). Analysis revealed that scan speed and power affected both nucleation and growth of SiC. A sharp cutoff value existed for power and scan speed below which no 3C-SiC was formed, suggesting that a critical power density is required to initiate nucleation of 3C-SiC. Within the range of parameters that allow 3C-SiC formation, we further studied the printed structural resolution using optical microscopy (fig. S3). Both the width and the depth of the converted lines/trenches after a single laser line scan (Fig. 3, A and B) could be tuned by either the laser power or the scan speed, indicating controllable fabrication of a semiconductor/elastomer composite.

We sought not only to understand the material properties but also to explore the utility of this fabrication technique in 2D and 3D printing of semiconductors. Figure 3C shows an example of a vectorized outline of the painting *The Angelus* printed over PDMS. Raman mapping of a selected area [dashed square in Fig. 3C (right)] displayed a photoluminescent (PL) pattern (Fig. 3D), with the spectrum centered at 691.3 nm (Fig. 3E). As the PL pattern is overlaid with the printed 3C-SiC outline, we attribute this PL signal to the doping and/or crystal defects in 3C-SiC (*22*).

For 3D printing, we used a layer-by-layer technique (Fig. 3, F and G), which is based on laser-assisted sidewall cutting/conversion and multilayer fusion. Following the formation of one layer of SiC structure over the cut PDMS sidewall, we applied a fresh layer of PDMS on top for additional SiC conversion in the new layer. Interlayer SiC fusion was readily achieved as the laser cutting/conversion reached the bottom of the new PDMS layer, producing a "welded" SiC construct. The 3D integrated SiC can be released from the PDMS matrix using Piranha etching. This technique is unique, as it does not use photopolymerizing agents and can be performed in a solid state (*23*).

Pseudocapacitive nature of 3C-SiC electrodes

We studied device applications for the printed 3C-SiC/graphite/PDMS composite. To explore the electrochemical properties of 3C-SiC, we prepared an electrode by electrically connecting the graphitic side of a scratched SiC/graphite patch to a copper wire using silver paste (fig. S4A). We then sealed the device so that only a confined surface of the densely packed SiC was exposed to the electrolyte (fig. S4A).

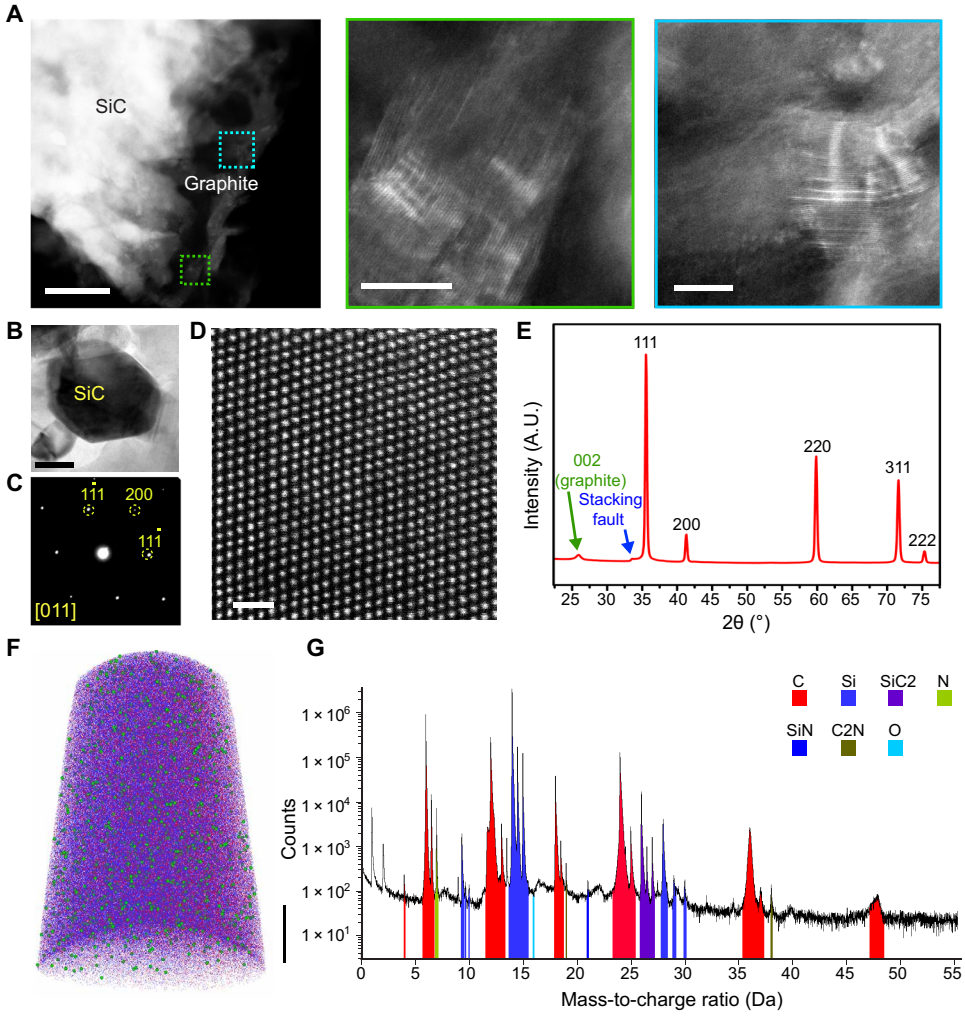

Fig. 2. Structural analysis of laser-printed SiC using electron microscopy shows the formation of a graphite layer underneath. (**A**) HAADF-STEM image revealing a porous graphitic surface integrated with SiC. Higher-magnification images reveal layered graphite structures in the regions marked in blue and green. (**B**) Microtomed section of 3C-SiC with its diffraction pattern (**C**) taken on [011] indexing zone. (**D**) HAADF-STEM image showing cubic SiC lattice. (**E**) X-ray diffraction revealing a 3C polytype of SiC with stacking faults and graphite layer beneath. (**F**) An atom probe reconstruction of a 3C-SiC sample revealing nitrogen doping. Elemental mapping: red, C; blue, Si; and green, N. (**G**). Mass spectrum from APT indicating nitrogen present in SiC lattice and its bonding with carbon and silicon atoms. Scale bars, (A) 0.1 μm (left), 10 nm (middle), 10 nm (right); (B) 100 nm; (D) 1 nm; (F) 20 nm. A.U., arbitrary units.

We characterized the devices using cyclic voltammetry (CV) in phosphate-buffered saline (PBS). The skewed square-like shape of the cyclic voltammogram and the decreasing trend of differential capacitance (i.e., from 6.28 to 4.67 mF/cm^2 and to 3.50 mF/cm^2, with an increasing scan rate from 50 to 100 mV/s and to 200 mV/s) suggest pseudocapacitive charging in 3C-SiC (*24*). Moreover, we observed that the differential capacitances are ~3 orders of magnitude greater than those for intrinsic 3C-SiC (prepared from SiC wafer) and a glassy carbon electrode (fig. S4, B and C) (*7*, *25*, *26*). The enhanced double-layer capacitance in nitrogen-doped 3C-SiC over standard intrinsic 3C-SiC may be attributed to its doping, crystal morphology and defects, and the electrochemical contributions of other components in the composite. This idea was reinforced by electrochemical impedance measurements, which revealed that charge transfer resistance of doped 3C-SiC crystals was ~4 orders of magnitude less than that of undoped 3C-SiC (fig. S4, D and E). Given the high surface sensitivity in electrochemical performance, the potential role of oxide defects as observed in x-ray photoelectron spectroscopy (XPS) (fig. S5) must also be noted (*27*). Nevertheless, such an enhanced double-layer capacitance and reduced charge transfer resistance would facilitate improved electrochemical coupling between composite surface and cells and tissues in biological modulation experiments.

Flexible electrochemical electrodes for heart pacing

We next printed and tested SiC-based flexible bioelectronic devices for tissue stimulation (Fig. 4). We fabricated two types of electrodes by printing zigzag or other curvilinear patterns on a PDMS layer with two different laser powers (Fig. 4A). A graphite layer formed in situ underneath the 3C-SiC acts as an interfacing electrode with excellent conductivity (Fig. 4B). Figure 4C highlights these composites as ready-to-use stimulation devices. Lower laser power facilitated partial ablation and creation of a surface electrode, while higher laser power created a cut-through sidewall electrode (Figs. 1A and 4, A and C). The devices were connected to a copper wire using silver

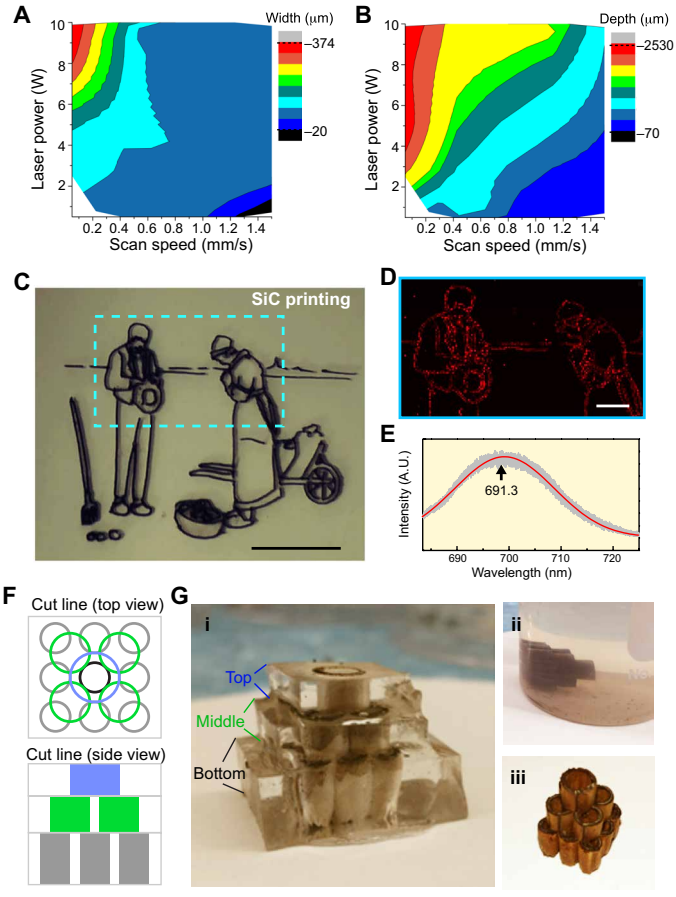

Fig. 3. Laser-printed SiC can form 2D and 3D structures. (**A**) Laser printing resolution determined by optical microscopy as a function of laser power and scan speed, represented as a contour plot. (**B**) Laser printing depth determined by optical microscopy as a function of laser power and scan speed, represented as a contour plot. (**C**) A painting that was vectorized and printed on PDMS. Scale bar, 1 cm. (**D**) Raman mapping of nitrogen defect luminescence on a printed pattern revealing SiC. Scale bar, 2 mm. (**E**) Nitrogen defect luminescence Raman spectrum of 3C-SiC. (**F**) Multilayer vector design for 3D printing. (**G**) Layer by layer printing method to obtain a stable 3D integrated structure. Photo credit: Jaeseok Yi, the University of Chicago. (i) Welding of subsequent layers, (ii) PDMS Piranha etching, and (iii) freestanding SiC-graphite structure.

paste, and all electrical contacts were sealed such that only the SiC surface was exposed to the electrolyte. To demonstrate the benefit of using these flexible electrodes in bioelectronics, we tested them in an ex vivo isolated heart that constantly displayed volume and shape changes (Fig. 4D). We mounted a viable contracting rat heart on Langendorff apparatus and placed the flexible SiC devices against the left and right ventricles (Fig. 4D). We then delivered electrical stimulation to the heart via the interfacing devices. Before stimulation, the slow atrioventricular node rhythm of 1.5 to 2 Hz could be observed in electrocardiography (ECG) and left ventricular pressure (LVP) recordings (Fig. 4, E and F). Upon electrical stimulation, the heart rate immediately synchronized to that of the stimulation rate. As the electrical stimulation clearly distorted the ECG signal due to the electrical artifact, we also used LVP recordings that showed the clear overdrive pacing effect of the stimulation. As expected, when electrical stimulation ceased, the heart resumed its slow atrioventricular node rhythm. This experiment indicates that the SiC/graphite/PDMS composite is fully applicable for tissue or organ modulation. The composite displays low electrode impedance and maintains its flexibility and integrity during the device operation.

Photoelectrochemical characteristics of 3C-SiC

As noted, the surface and composition of the device will influence its electrochemical properties, which are critical for formation of functional biointerfaces. We used micropipette-based photocurrent measurements to determine the electrochemical activities that the SiC surface displays upon optical excitation (Fig. 5, A and B). The recorded photocurrent showed primarily a negative sign (Fig. 5B), indicating that the printed 3C-SiC exhibited a photoanodic output (*4*). The photoanodic activity from 3C-SiC and 3C-SiC-MnO_x is consistent with the n-type nature of the nitrogen-doped 3C-SiC and the upward band bending at the electrolyte interface (Fig. 5A) (*28*). Besides, this photoanodic behavior from the laser-produced doped 3C-SiC was in stark contrast with the pure photocapacitive behavior exhibited by the intrinsic 3C-SiC wafer (fig. S6A). Electroless deposition of MnO_x ($x \sim 2$) onto the 3C-SiC surface leads to ~10-fold enhancement of the photoanodic reaction (fig. S6B). A direct photoelectrical contribution from the graphitic layer beneath the 3C-SiC can be ruled out (fig. S6C), although the graphitic layer may serve as a collector for photogenerated electrons (which would promote the photoanodic reaction on the SiC surface).

Oxidation of water to hydrogen peroxide (H_2O_2) is one potential chemical reaction behind the observed photoanodic current (Fig. 5A). To test the hypothesis of H_2O_2 production, we undertook fluorescence-based kinetics studies (Fig. 5C and fig. S7). For 3C-SiC, fluorescence measurements confirmed production of H_2O_2 and the kinetics showed its saturation over time (Fig. 5C and fig. S7). However, for 3C-SiC-MnO_x, H_2O_2 production continued to increase linearly. While MnO_2 is known to readily oxidize H_2O_2 to oxygen (*29*) and may assist in a complete water oxidation reaction instead (*30*), the MnO_x particles produced over SiC surfaces may yield different reactivities. While elucidation of the exact mechanism for this catalytic photoreaction requires further studies of the SiC-MnO_2 junction and interface behaviors, our current results highlight that the photogenerated H_2O_2 could affect the biointerfaces in different ways: (i) 3C-SiC could provide a therapeutic dose of H_2O_2 suitable for biological modulation, and (ii) 3C-SiC-MnO_2 could provide a lethal dose, useful for antibacterial applications (see results in fig. S8).

3C-SiC as a "dry" H_2O_2 reservoir for muscle stimulation

In the vascular system, H_2O_2 and other reactive oxygen species play an important role in the modulation of smooth muscle cells (*31*). Endothelial cells that form the lining of arteries and veins sense pressure and use nitric oxide to signal smooth cells to regulate their contraction-relaxation cycles (*32*). However, studies have revealed that the direct addition of H_2O_2 could also elicit a similar response via regulation of inositol triphosphate receptors (IP3R) (Fig. 5D) (*33*). Thus, we studied the calcium signals of individual cells in an ensemble of smooth muscle cells following photoelectrochemical stimulation from cell-interfaced 3C-SiC. We analyzed the calcium signals of individual cells in the region of stimulation and classified the cells as stationary or oscillatory. Stationary cells were those in which the cellular response was generally below the action potential threshold; stationary cells only contracted occasionally (~1 contraction cycle per 2 to 3 min). Oscillatory cells were those in which the cellular response was generally above the action potential

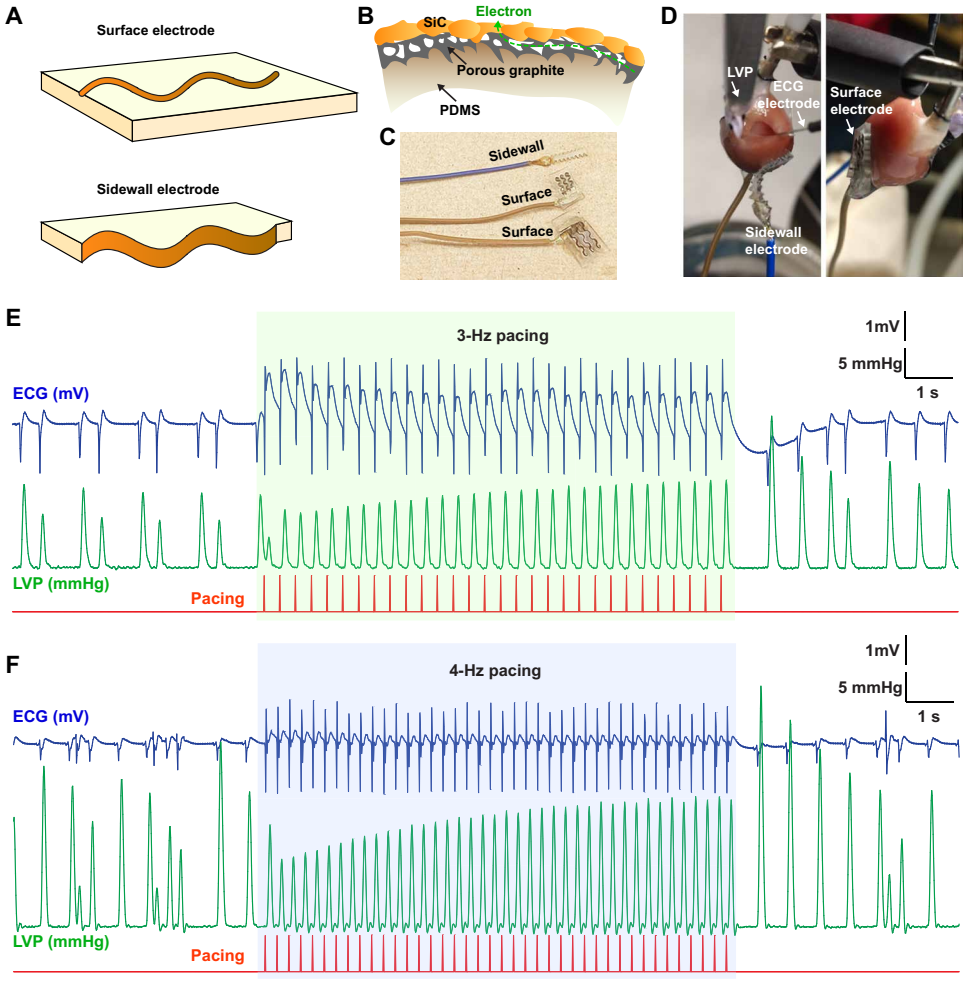

Fig. 4. Electrical heart pacing with flexible electrodes. (**A**) Schematic depiction of surface interfacing and side interfacing electrodes that can be printed by varying the power and scan speed. A complete through-cut creates side electrodes. (**B**) Schematic illustration showing porous graphite structure underlying SiC, serving as a contact for electrical interfacing. (**C**) Photographs showing sidewall and surface printed electrodes on PDMS for interfacing with the isolated heart in cardiac pacing experiments. Photo credit: Lingyuan Meng, the University of Chicago. (**D**) Photographs illustrating sidewall and surface electrodes interfacing with an isolated rat heart in a Langendorff setup. Photo credit: Vishnu Nair, the University of Chicago. (**E** and **F**) Representative traces from cardiac pacing experiments on an isolated heart. An electrical stimulus is supplied through two SiC electrodes at a frequency of 3 Hz (E) and 4 Hz (F). Both electrical stimulations are successful as observed by in-phase ECG signals and LVP recording.

threshold; oscillatory cells were more electrically and mechanically active (~3 to 4 contraction cycles per minute) (*34*, *35*). Upon photoelectrochemical stimulation, exogenous H_2O_2 was made available, which triggered distinct responses in stationary and oscillatory cells. Stationary cells responded to the stimulation (1 ms of 592 nm at 29 mW) with a calcium spike (Fig. 5E, i). Oscillatory cells responded to H_2O_2 in three ways, depending on whether the stimulation happened during their relaxed state (Fig. 5E, ii), immediately after contraction (Fig. 5E, iii), or just after the cell had reached a relaxed state (Fig. 5E, iv). The three responses were a phase shift (delay in next firing) in oscillation (Fig. 5E, ii), a transient increase in oscillation frequency (Fig. 5E, iii), or an increase in oscillation frequency followed by damping to higher calcium level (Fig. 5E, iv), respectively. These perturbations in oscillatory responses are consistent with experimental and theoretical studies of the behavior of smooth muscle following an increase in IP3 levels (*35*).

To explain the smooth muscle cell response, we propose that exogenous H_2O_2 potentially increases IP3 levels through activation of G protein–coupled receptors (GPCRs) or receptor tyrosine kinases (RTKs) (*31*, *34*, *36*, *37*). GPCR or RTK activation leads to an increase in cytosolic IP3, which, along with cytosolic calcium, regulates IP3R in a cyclic fashion (*34*). Such a biphasic regulation of IP3R by cytosolic calcium leads to oscillations in cytosolic calcium and transmembrane chloride current (*34*). The opening of this transmembrane chloride channel causes depolarization via the uptake of exogenous calcium and the release of calcium from internal stores such as the endoplasmic or sarcoplasmic reticulum (*33*–*35*). Combining these known facts with our observations of cellular calcium perturbation, we suggest that an IP3-based signaling mechanism is involved. The ability of 3C-SiC–produced H_2O_2 to modulate smooth muscle contraction cycles through an IP3-mediated pathway is analogous to the native mechanism in which endothelial cells communicate through nitric oxide. To demonstrate the potential of integrating laser-produced SiC into a cell culture platform, we stimulated a sheet of smooth muscle cells using a printed trench-like SiC device

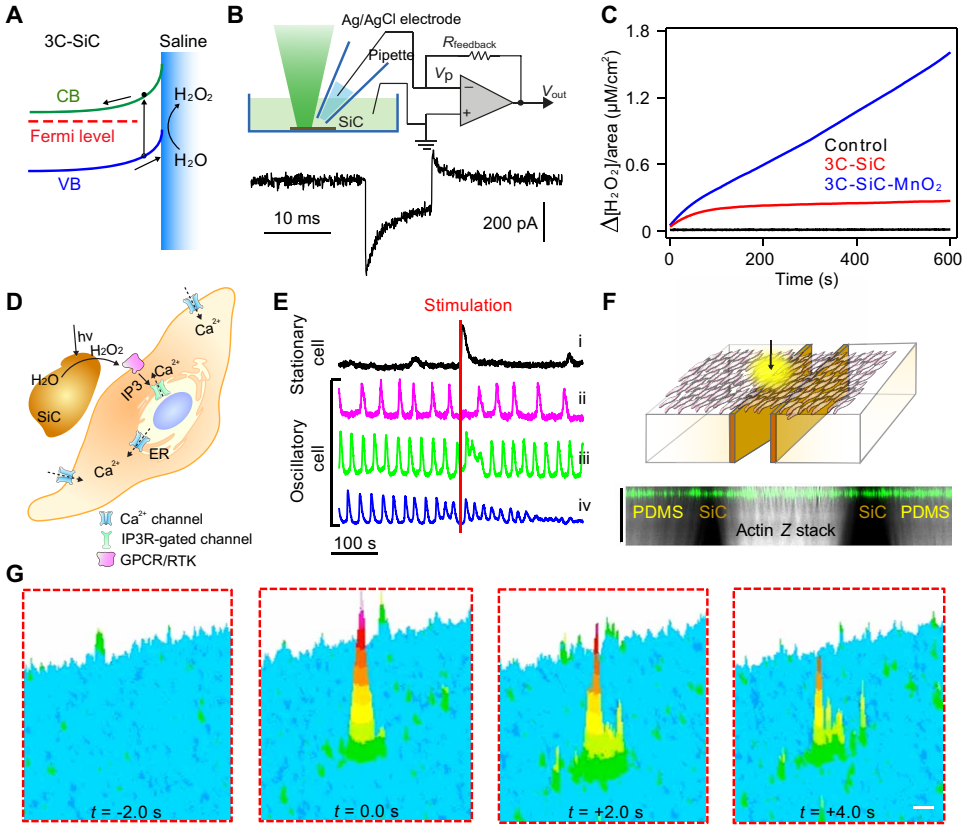

Fig. 5. Stimulation of primary human aortic smooth muscle cells with SiC biomimicry. (**A**) The n-doping in 3C-SiC and subsequent band bending suggests the possibility of pure oxidation reactions after photostimulation. (**B**) Schematic of a photocurrent measurement setup (top) and a representative trace of a 3C-SiC photoresponse during a 10-ms light-emitting diode (LED) pulse of 375 nm revealing a photoanodic oxidation reaction. (**C**) Fluorescence kinetics measurements on 3C-SiC and 3C-SiC-MnO_2 confirm oxidation of water to H_2O_2 and show the relative concentration of H_2O_2 produced by oxidation of water per square centimeter of material irradiated with light. (**D**) Schematic illustration of an exogenous H_2O_2 signaling pathway in smooth muscle cells. Exogenous peroxides cause increased activation of inositol triphosphate receptor (IP3R), inducing the release of calcium from internal stores such as endoplasmic reticulum (ER)/sarcoplasmic reticulum (SR) and uptake of exogenous calcium. (**E**) Representative traces of the differing calcium responses depending on the stimulation timing with respect to a contraction cycle. (**F**) Schematic of a device level implementation on a smooth muscle cell ensemble with a microscopy *Z* stack (see also fig. S9 for *XY* view). Scale bar, 100 μm along the *Z* axis only. (**G**) 3D heatmaps showing a calcium wave propagating from the stimulation point in the cell ensemble. Scale bar, 50 μm (movie S1). CB, conduction band; VB, valence band; GPCR, G protein–coupled receptor; RTK, receptor tyrosine kinase.

(Fig. 5F) or freestanding 3C-SiC particles (fig. S9, B and C). Our results revealed an overall increase in calcium levels and its propagation into adjacent cells as a calcium wave (Fig. 5G and movie S1). In the ensemble of smooth muscle cells, the cellular level calcium response manifested in different ways, as described above (Fig. 5E). We studied the correlation between calcium signals from individual smooth muscle cells in the ensemble. Our results revealed a post-stimulation increase in synchronization, suggesting enhanced contractility of the smooth muscle sheet (fig. S9, D and E, and movie S2). These preliminary results suggest the therapeutic utility of our device in remote control of, e.g., vasoconstriction in trauma surgeries or sphincter contraction after chronic spinal cord injury (*38*, *39*).

CONCLUSION AND OUTLOOK

This work demonstrates 2D and 3D laser writing of nitrogen-doped 3C-SiC over PDMS substrates. The 3C-SiC layer establishes a seamless hard-soft interface with PDMS through a spongy graphite layer. We developed SiC-based flexible devices as pseudocapacitively coupled stimulation electrodes for isolated hearts and photoelectrodes for localized H_2O_2 production for mammalian and microbial cell modulation. Our results suggest the future utility of seamlessly integrated semiconductor/elastomer composites for organ-on-a-chip or organoid-on-a-chip research or microfluidic systems where photoelectrochemical or electrochemical capabilities are needed. Future studies will include mechanistic understanding of the charge transfer at the SiC/graphite and SiC/MnO_x interfaces and surfaces and the growth mechanism for 3C-SiC under different laser ablation. The precise electrochemical mechanism of hydrogen peroxide production and signal transduction pathway in cells also need to be studied.

MATERIALS AND METHODS

Synthesis of PDMS matrix

PDMS was prepared using a commercially available SYLGARD 184 kit. The polymer and curing agent were mixed in a 10:1 ratio by weight and degassed in vacuum. This was followed by vacuum degassing

and curing at 80°C for 8 hours. Only properly degassed, bubble-free, clear samples were used in all of the experiments. Substrate thickness was between 0.5 and 5 mm.

Laser ablation of PDMS to SiC

PDMS layers were mounted on an aluminum comb (with a supporting layer of glass or polystyrene petri dish) and laser written with a CO_2 laser of 10.6-μm wavelength, up to a power of 50 W (VLS 4.60 manufactured by Universal Laser Systems with flame retardant nitrogen purging) with a 100-μm spot size. The pattern for writing was generated as a vector image in CorelDRAW and printed using VLS 4.60 software. For certain material property studies, writing was performed in vector cutting mode with parameters of 100% power (50 W), 1000 points per inch, and speed of 0.254 mm/s. For pattern printing, the power was lowered to 2.5% (1.25 W) and speed of 0.254 mm/s. (Warning: Using no supporting layer or thin samples of PDMS would cause the laser to hit the aluminum comb below and melt and even contaminate your samples.) Depending on the power of the laser, the PDMS sample may be cut across with regions of SiC on either side. For circuit printing, we used lower power (5%) to create the circuit as a thin layer. For crystal structure and bulk analysis, we used full power (100%) so that a larger quantity of sample was converted. Power only affects conversion along the vertical direction; it does not affect the horizontal or vertical composition of transformed material. Etching of the 3D structure was performed using Piranha etch [H_2SO_4: 30% H_2O_2, 3:1 (v/v); ThermoFisher Scientific] for an hour.

Processing SiC for characterization and analysis

Samples prepared with 100% power were generally used for crystal structure and property analysis and for direct integration with cells via dispersion of the crystals in growth media. However, before these processes, the crystals were purified. The SiC along with the graphite layer was cut out from the PDMS matrix using a razor blade. The sample was then washed in toluene (ThermoFisher Scientific) for 5 min to remove any organic components present in the material. Following this, the sample was immersed in isopropyl alcohol (ThermoFisher Scientific) for 5 min and then in deionized (DI; 18.2 megohm) water for 5 min. After this sequential washing, the samples were dipped in 1:1 HF:HNO_3 (Sigma-Aldrich) for 5 min to remove any silica and surface organics. Last, the samples were washed in DI water, dried using a nitrogen blow dry process, and oxygen plasma cleaned at 200 W for 3 min (PE-100 Benchtop Plasma System). After the final step, the SiC synthesized from pure PDMS appeared yellow (fig. S1g).

Electroless deposition of manganese dioxide

Electroless deposition on the purified clean SiC surface was carried out using a solution of 0.25 M $KMnO_4$ (Sigma-Aldrich) in 0.5 M H_2SO_4 (Sigma-Aldrich). The samples were washed in a water and ethanol (1:1) mixture and then kept dipped in the above mixture for 10 min. The samples were then washed in water and dried using a nitrogen blow dry process.

Electron microscopy and sample preparation

Sample preparation for TEM and STEM

The crystals were scratched using a tweezer, and the resulting powder was loaded into a resin mold. The mold was then filled with epoxy resin, degassed in vacuum, and baked at 60°C overnight for embedment. The crystals were microtomed (Leica UC6) into 100-nm sections and loaded on 200 mesh copper grids, which were stored in a vacuum desiccator. TEM and SAED patterns were collected on a JEOL 3010F operating at an accelerating voltage of 300 kV with a LaB_6 filament.

Scanning transmission electron microscopy

STEM was performed on a JEOL ARM 200CF (Cs corrected) with a field emission gun at an accelerating voltage of 200 kV. STEM was performed on each area after a 200-kV, 30-min beam shower at the spot to remove any adsorbed hydrocarbon contaminants. Scanning electron microscopy and energy-dispersive X-ray spectroscopy (EDS) were performed on TESCAN LYRA3 system equipped with Dual Oxford Instruments X-Max-80 silicon drift x-detectors for EDS (fig. S10).

X-ray scattering

X-ray scattering measurements on SiC were carried out on a 17-BM beamline at the Advanced Photon Source, Argonne National Laboratory.

Indexing of SAED and fast Fourier transform patterns

3C-SiC structures were generated in a CrystalMaker 2.0 using existing reported structures, and patterns were indexed using Crystal Diffract 2.0.

Materials optical microscopy

To analyze the resolution of printed features, bright-field color images were taken with an Olympus LEXT OLS5000 Microscope.

X-ray photoelectron spectroscopy

XPS was performed on a ThermoFisher Scientific ESCALAB 250Xi equipped with an electron flood gun and argon ion sputter gun. XPS measurements were carried out using an Al Kα x-ray source of 1.487-keV energy and a spot size with a diameter of 500 μm.

APT and sample preparation

Figure S1 shows the general workflow of APT sample preparation. SiC crystals were first cut and lifted using focus ion beam (FIB) milling. The samples were sputter-coated with 50-nm nickel to prevent charging during further FIB milling processes. The crystals were then milled into small lamellas on a FEI Helios. These lamellas were transferred to silicon microposts using a micromanipulator and milled down to needles for APT. The needles were mounted into a LEAP 5000 XS (Cameca) and charged to a potential between 1 and 6 kV. Following this, the surface atoms were evaporated using 355-nm laser pulses of 30 pJ at a frequency of 250 kHz in a chamber maintained at 30 K and 2×10^{-11} torr. The 3D structures were reconstructed and analyzed using Cameca's integrated visualization and analysis software (IVAS) 3.8 code.

Photocurrent measurements

Photocurrent measurements were performed by single-channel voltage clamp recordings on a patch-clamp amplifier (Axopatch 200B) setup. The material of interest was immersed in 1× PBS (ThermoFisher Scientific) in a petri dish and focused on using a microscope (Olympus BX61WI) with a water immersion lens [20×/0.5 NA (numerical aperture)]. Light pulses were delivered through the microscope using a 375-nm light-emitting diode (LED) source (Thorlabs M375L4; ~500-μm spot size). Electrical pulses were delivered to these

light sources using a digitizer (Molecular Devices, Digidata 1550). For photocurrent measurements, glass pipettes of ~1 megohm were pulled (Sutter Instrument, P-97) and their tips were lowered and focused onto the same optical plane (gap of ~2 μm) as the material surface before the stimulation pulse was applied. The voltage clamped currents were recorded in parallel with the stimulation pulse at various holding current levels. The data were analyzed, and the nature of the photocurrents was determined using a previously developed method (*4*).

PL measurements

Raman measurements of PL from SiC were performed for laser-written patterns and crystals to understand the presence of defect-related emissions in the system. PL measurements were carried out using a 473-nm excitation laser and detection in a back-scattered geometry with a 50×/0.5 NA objective and 600 grooves/mm grating, under ambient conditions. Point spectra were collected for crystals, and mapping was carried out on laser-printed patterns. Raman measurements were carried out on a Horiba LabRAM HR Evo Confocal Raman.

Fluorescence kinetics

Fluorescence kinetics experiments were carried out on SiC crystals to understand the photo redox species produced in solution. Amplex Red peroxide/peroxidase kit was used according to the manufacturer's instructions. To use the same excitation for both the dye emission and the photoanodic process, we attached the crystals facing the excitation source and on the inner face of the cuvette such that the entire fluorescent signal was transferred to the detector at 90° without any obstruction. The beam of the spectrometer was rectangular with ~0.21-cm^2 area.

Electrochemical measurements and *I-V* characteristics

A purified piece of graphite-SiC layer was isolated and attached to a wire using conductive silver paste on the graphite side. The wire contact and the graphite side and edges were sealed using nail polish or epoxy and dried overnight such that only the SiC crystals were exposed to the electrolyte. The projected area of the SiC crystals exposed was ~0.09 cm^2, that of the standard glassy carbon (CHI104) electrode was ~0.07 cm^2 and that of an undoped 3C-SiC wafer (MTI Corporation, SiC-3CP-a-4-13-05050525-2.2) was 0.25 cm^2. CV was carried out at scan rates of 200, 100, and 50 mV/s from −0.7 to 0.0 V in 1× PBS on a Bio-Logic SP-200 potentiostat. The current was scaled with respect to the area of electrode and the area in a cycle of CV estimated by integration in Origin Pro 8.0. The differential capacitance of the electrode was calculated using the equation $\partial C/\partial A = (1/f\Delta V) \int J\, dV$, where J is the current density, V is the potential, f is the scan rate, and ΔV is the potential window of scan. The *I-V* characteristics were measured by a Keithley source meter 2636A. Electrochemical impedance measurements were carried out from 3 MHz through 1 kHz with 10 points per decade and 10 averaging cycles per measurement. The Nyquist plots were fit using a Randles circuit to obtain the resistance of charge transfer.

Isolated heart stimulation experiment

Device fabrication

A PDMS film was prepared with a thickness of 100 μm on a glass slide by spin coating followed by curing at 100°C for 30 min. The PDMS film was mechanically peeled off and transferred onto acrylic. In a typical conversion of PDMS to SiC, a laser scan with a predefined pattern at 5% power (2.5 W), 1000 points per inch, and speed of 0.254 mm/s was performed. Residual PDMS film maybe removed by mechanical peel-off or chemical etching. Silver paste or solder was used to connect the copper wires with the devices. To passivate the connection points, either PDMS or nail polish was used.

Animal experiment

All animal procedures were conducted in complete compliance with and with approval from the University of Chicago Institutional Animal Care and Use Committee. Adult rats (CD) were heparinized via intraperitoneal injection (1000 IU/kg), and an open-drop exposure to isoflurane in a bell jar configuration was used for anesthesia. The chest was opened, and the hearts were immediately excised and placed in ice-cold Hanks' balanced salt solution buffer. The aorta was cannulated in preparation for use in a Langendorff setup. Oxygenated Hepes-buffered Tyrode's solution (containing 126 mM NaCl, 5.4 mM KCl, 10 mM glucose, 10 mM HEPES, 1 mM $MgCl_2$, 2 mM $CaCl_2$, 1.2 mM $MgSO_4$, and 0.39 mM NaH_2PO_4; bubbled with 99.5% O_2; pH titered to 7.3 by 2 M NaOH) was perfused through the cannulated aorta. The perfusion was passed through a heating coil and bubble trap (Radnoti), and the hearts were placed in a water-jacketed beaker (ThermoFisher Scientific) to maintain the temperature at 37°C. The perfusion pressure, which was monitored using a BP-100 probe (iWorx), was set to 80 to 100 mmHg by an intravenous bag set at an appropriate height. A water-filled balloon was inserted to the left ventricle and connected to a BP-100 probe (iWorx) to monitor LVP. For ECG recordings, a needle electrode was positioned on the apex and the aorta was clamped and connected to a C-ISO-256 preamplifier (iWorx). All recordings (ECG, LVP, and perfusion pressure) were amplified using an IA-400D amplifier (iWorx) and interfaced with a PC using a Digidata 1550 digitizer with pCLAMP software (Molecular Devices). To lower the heart rate, the atriums were removed. Then, two PDMS devices with SiC patterns were positioned on the left and right ventricular wall and connected to an isolated constant current generator (SI-100R, iWorx) and a waveform generator for heart pacing. ECG and LVP recordings were used to assess beating frequency of the hearts before and during the stimulation.

Human aortic smooth muscle culture

Primary human aortic smooth muscle cells were purchased from the American Type Culture Collection (ATCC; PCS-100-012) and cultured in Medium 231 (Life Technologies), 500 ml of which was supplemented with 25 ml of growth supplement (smooth muscle growth supplement; Life Technologies) and sodium L-ascorbate (50 μg/ml; Sigma-Aldrich) for extracellular matrix secretion. The cells were seeded at a density of 1.25×10^4 per ml and used within the first three passages. The glass and PDMS surfaces were coated with collagen before seeding. The PDMS surfaces were oxygen plasma cleaned at 200 W for 10 min immediately before seeding collagen to make the surface hydrophilic.

Particle level biointerface studies

For biointerface studies with 3C-SiC, the crystals were scratched out from the graphite layers and washed in 100% ethanol. They were sterilized, dried overnight under an ultraviolet lamp in a bio-hood, and then redispersed in the complete media of the required cell type by bath sonication. The medium was changed for the required culture to the one with dispersed SiC within 24 hours of culture

initiation. Stimulation experiments were performed within the next 24 hours.

Immunofluorescence staining

Cell cultures were fixed with 4% paraformaldehyde in PBS for 10 min and then washed in PBS thrice. Following this, they were permeabilized with 0.5% Triton X-100 for 10 min and washed in PBS thrice. After the cells were fixed and permeabilized, they were incubated in a blocking solution of 3% bovine serum albumin in PBS for 60 min, following which ActinGreen 488 ReadyProbes (2 drops/ml; Invitrogen) was added to the blocking solution. The solution was incubated for another 30 min with the actin stain before washing and imaging in PBS.

Calcium imaging

Calcium imaging was done using Fluo-4 AM (Invitrogen), which was made into a 50 μM stock solution in Pluronic F-127, which is in 20% dimethyl sulfoxide (Invitrogen). Cell were incubated with 2 μM Fluo-4 AM in media for 30 min and washed after incubation with media. Cells were further incubated for 15 min in media before imaging. Calcium imaging was carried out at a rate of 3.8 Hz with a resolution of 512 × 512 pixels per frame on a Leica SP5 STED-CW confocal microscope in a 37°C incubator.

Confocal stimulation experiments

Point stimulation experiments were carried out in the FRAP mode of a Leica SP5 STED-CW confocal microscope with a 592-nm laser. Stimulation was carried out for 1 ms and at varying powers.

Smooth muscle stimulation data analysis

Smooth muscle calcium data were analyzed using LAS X (Leica application software). The regions of interest were drawn around smooth muscle regions near and away from stimulation. Raw calcium traces were used to study biophysical understanding of peroxide-induced perturbations on calcium oscillations. For device stimulation studies, the calcium channel videos were converted into tiff stacks using Fiji-ImageJ. The stacks were converted into $\Delta F/F$ images, and the surface plots were generated on Fiji-ImageJ. The $\Delta F/F$ data were baseline corrected for bleaching effects using a convex envelope method on PeakCaller software package (*40*). The processed $\Delta F/F$ curves were further processed on PeakCaller to generate the synchronization matrices, mean synchronization index, calcium waveforms, and raster plots. PeakCaller package was run on MATLAB R2018b engine. Phase synchronization is advantageous, as it is time resolved and only sensitive to phases and not the amplitude. If we have two continuous-time calcium signal $x(t)$ and $y(t)$, then we would need to determine their instantaneous phases φ_X and φ_Y, respectively. This is done by taking the Hilbert transform of the continuous-time signal given by $\tilde{x}(t) = \frac{1}{\pi}\int_{-\infty}^{\infty} \frac{x(t')}{t - t'}\, dt'$. The Hilbert phase can be obtained by $\tan^{-1}\left(\frac{\tilde{x}(t)}{x(t)}\right)$. Once the Hilbert phase is obtained, the mean synchronization index can be calculated between every neuron pair for N time steps as $\left|\frac{1}{N}\sum_{j=1}^{N} e^{i(\phi_x(t_j) - \phi_y(t_j))}\right|$. The values of mean synchronization index vary between 0 and 1, one being the most synchronized and zero being the least.

Antibacterial experiments

Escherichia coli MG1655 was obtained from the ATCC. *E. coli* was cultured to log phase in Luria-Bertani (LB) media and harvested by centrifugation at 3000 rpm. It was then washed twice with PBS and suspended in LB medium, PBS, or DI water to ~106 colony-forming units/ml separately. 3C-SiC-MnO_2 crystals were added to this bacteria culture and mixed uniformly. Photocatalytic disinfection was performed using a white LED of 5-mW power for 24 hours. Bacteria concentrations were measured after 24 hours of illumination using standard spread-plate techniques. Each sample was serially diluted, and each dilution was plated in triplicate onto LB plates and incubated overnight at 37°C. Experiments for disinfection were also conducted in duplicate with 3C-SiC-MnO_2 under dark conditions (control 1) and without 3C-SiC-MnO_2 under LED light illumination (control 2).

SUPPLEMENTARY MATERIALS

Supplementary material for this article is available at http://advances.sciencemag.org/cgi/content/full/6/34/eaaz2743/DC1

View/request a protocol for this paper from *Bio-protocol*.

REFERENCES AND NOTES

1. R. Ye, X. Han, D. V. Kosynkin, Y. Li, C. Zhang, B. Jiang, A. A. Martí, J. M. Tour, Laser-induced conversion of teflon into fluorinated nanodiamonds or fluorinated graphene. *ACS Nano* **12**, 1083–1088 (2018).
2. D. X. Luong, K. Yang, J. Yoon, S. P. Singh, T. Wang, C. J. Arnusch, J. M. Tour, Laser-induced graphene composites as multifunctional surfaces. *ACS Nano* **13**, 2579–2586 (2019).
3. M. G. Stanford, J. T. Li, Y. Chyan, Z. Wang, W. Wang, J. M. Tour, Laser-induced graphene triboelectric nanogenerators. *ACS Nano* **13**, 7166–7174 (2019).
4. Y. Jiang, X. Li, B. Liu, J. Yi, Y. Fang, F. Shi, X. Gao, E. Sudzilovsky, R. Parameswaran, K. Koehler, V. Nair, J. Yue, K. Guo, Y. Fang, H.-M. Tsai, G. Freyermuth, R. C. S. Wong, C.-M. Kao, C.-T. Chen, A. W. Nicholls, X. Wu, G. M. G. Shepherd, B. Tian, Rational design of silicon structures for optically controlled multiscale biointerfaces. *Nat. Biomed. Eng.* **2**, 508–521 (2018).
5. Y. Yang, Y. Song, X. Bo, J. Min, O. S. Pak, L. Zhu, M. Wang, J. Tu, A. Kogan, H. Zhang, T. K. Hsiai, Z. Li, W. Gao, A laser-engraved wearable sensor for sensitive detection of uric acid and tyrosine in sweat. *Nat. Biotechnol.* **38**, 217–224 (2020).
6. R. M. Torrente-Rodríguez, J. Tu, Y. Yang, J. Min, M. Wang, Y. Song, Y. Yu, C. Xu, C. Ye, W. W. IsHak, W. Gao, Investigation of cortisol dynamics in human sweat using a graphene-based wireless mhealth system. *Matter* **2**, 921–937 (2020).
7. K. J. Yu, D. Kuzum, S.-W. Hwang, B. H. Kim, H. Juul, N. H. Kim, S. M. Won, K. Chiang, M. Trumpis, A. G. Richardson, H. Cheng, H. Fang, M. Thompson, H. Bink, D. Talos, K. J. Seo, H. N. Lee, S.-K. Kang, J.-H. Kim, J. Y. Lee, Y. Huang, F. E. Jensen, M. A. Dichter, T. H. Lucas, J. Viventi, B. Litt, J. A. Rogers, Bioresorbable silicon electronics for transient spatiotemporal mapping of electrical activity from the cerebral cortex. *Nat. Mater.* **15**, 782–791 (2016).
8. Y. K. Lee, K. J. Yu, E. Song, A. Barati Farimani, F. Vitale, Z. Xie, Y. Yoon, Y. Kim, A. Richardson, H. Luan, Y. Wu, X. Xie, T. H. Lucas, K. Crawford, Y. Mei, X. Feng, Y. Huang, B. Litt, N. R. Aluru, L. Yin, J. A. Rogers, Dissolution of monocrystalline silicon nanomembranes and their use as encapsulation layers and electrical interfaces in water-soluble electronics. *ACS Nano* **11**, 12562–12572 (2017).
9. J. U. Lind, T. A. Busbee, A. D. Valentine, F. S. Pasqualini, H. Yuan, M. Yadid, S.-J. Park, A. Kotikian, A. P. Nesmith, P. H. Campbell, J. J. Vlassak, J. A. Lewis, K. K. Parker, Instrumented cardiac microphysiological devices via multimaterial three-dimensional printing. *Nat. Mater.* **16**, 303–308 (2017).
10. F. Molina-Lopez, T. Z. Gao, U. Kraft, C. Zhu, T. Öhlund, R. Pfattner, V. R. Feig, Y. Kim, S. Wang, Y. Yun, Z. Bao, Inkjet-printed stretchable and low voltage synaptic transistor array. *Nat. Commun.* **10**, 2676 (2019).
11. G. T. Burns, R. B. Taylor, Y. Xu, A. Zangvil, G. A. Zank, High-temperature chemistry of the conversion of siloxanes to silicon carbide. *Chem. Mater.* **4**, 1313–1323 (1992).
12. Y. Nakajima, S. Hayashi, A. Katayama, N. Nedyalkov, M. Terakawa, Femtosecond laser-based modification of PDMS to electrically conductive silicon carbide. *Nanomaterials (Basel)* **8**, 558 (2018).
13. P. Amorós, D. Beltrán, C. Guillem, J. Latorre, Synthesis and characterization of SiC/MC/C ceramics (M = Ti, Zr, Hf) starting from totally non-oxidic precursors. *Chem. Mater.* **14**, 1585–1590 (2002).
14. A. W. Weimer, *Carbide, Nitride and Boride Materials Synthesis and Processing* (Springer, 2012).
15. X. Zou, L. Ji, X. Lu, Z. Zhou, Facile electrosynthesis of silicon carbide nanowires from silica/carbon precursors in molten salt. *Sci. Rep.* **7**, 9978 (2017).

16. F. La Via, A. Severino, R. Anzalone, C. Bongiorno, G. Litrico, M. Mauceri, M. Schoeler, P. Schuh, P. Wellmann, From thin film to bulk 3C-SiC growth: Understanding the mechanism of defects reduction. *Mater. Sci. Semicond. Process.* **78**, 57–68 (2018).
17. W. F. Knippenberg, Growth phenomena in silicon carbide. *Philips Res. Rep.* **18**, 161–274 (1963).
18. N. W. Jepps, T. F. Page, Polytypic transformations in silicon carbide. *Prog. Cryst. Growth Charact.* **7**, 259–307 (1983).
19. P. Hu, S. Dong, X. Zhang, K. Gui, G. Chen, Z. Hu, Synthesis and characterization of ultralong SiC nanowires with unique optical properties, excellent thermal stability and flexible nanomechanical properties. *Sci. Rep.* **7**, 3011 (2017).
20. M. G. Walter, E. L. Warren, J. R. McKone, S. W. Boettcher, Q. Mi, E. A. Santori, N. S. Lewis, Solar water splitting cells. *Chem. Rev.* **110**, 6446–6473 (2010).
21. E. N. Mokhov, in *Crystal Growth*, V. Glebovsky, Ed. (IntechOpen, Rijeka, 2019).
22. H. W. Shim, K. C. Kim, Y. H. Seo, K. S. Nahm, E. K. Suh, H. J. Lee, Y. G. Hwang, Anomalous photoluminescence from 3C-SiC grown on Si(111) by rapid thermal chemical vapor deposition. *Appl. Phys. Lett.* **70**, 1757–1759 (1997).
23. R. D. Farahani, M. Dubé, D. Therriault, Three-dimensional printing of multifunctional nanocomposites: Manufacturing techniques and applications. *Adv. Mater.* **28**, 5794–5821 (2016).
24. Y. Zou, A. S. Walton, I. A. Kinloch, R. A. W. Dryfe, Investigation of the differential capacitance of highly ordered pyrolytic graphite as a model material of graphene. *Langmuir* **32**, 11448–11455 (2016).
25. V. Nair, B. Ananthoju, J. Mohapatra, M. Aslam, Photon induced non-linear quantized double layer charging in quaternary semiconducting quantum dots. *J. Colloid Interface Sci.* **514**, 452–458 (2018).
26. R. Trouillon, D. O'Hare, Comparison of glassy carbon and boron doped diamond electrodes: Resistance to biofouling. *Electrochim. Acta* **55**, 6586–6595 (2010).
27. M. Kim, H. Ju, J. Kim, Oxygen-doped porous silicon carbide spheres as electrode materials for supercapacitors. *Phys. Chem. Chem. Phys.* **18**, 3331–3338 (2016).
28. A. J. Bard, M. Stratmann, *Encyclopedia of Electrochemistry* (Wiley-VCH, 2006).
29. S.-H. Do, B. Batchelor, H.-K. Lee, S.-H. Kong, Hydrogen peroxide decomposition on manganese oxide (pyrolusite): Kinetics, intermediates, and mechanism. *Chemosphere* **75**, 8–12 (2009).
30. M. M. Najafpour, G. Renger, M. Hołyńska, A. N. Moghaddam, E.-M. Aro, R. Carpentier, H. Nishihara, J. J. Eaton-Rye, J.-R. Shen, S. I. Allakhverdiev, Manganese compounds as water-oxidizing catalysts: From the natural water-oxidizing complex to nanosized manganese oxide structures. *Chem. Rev.* **116**, 2886–2936 (2016).
31. F. R. González-Pacheco, C. Caramelo, M. Á. Castilla, J. J. P. Deudero, J. Arias, S. Yagüe, S. Jiménez, R. Bragado, M. V. Álvarez-Arroyo, Mechanism of vascular smooth muscle cells activation by hydrogen peroxide: Role of phospholipase C gamma. *Nephrol. Dial. Transplant.* **17**, 392–398 (2002).
32. S. Dimmeler, I. Fleming, B. Fisslthaler, C. Hermann, R. Busse, A. M. Zeiher, Activation of nitric oxide synthase in endothelial cells by Akt-dependent phosphorylation. *Nature* **399**, 601–605 (1999).
33. E. Santiago, B. Climent, M. Muñoz, A. García-Sacristán, L. Rivera, D. Prieto, Hydrogen peroxide activates store-operated Ca^{2+} entry in coronary arteries. *Br. J. Pharmacol.* **172**, 5318–5332 (2015).
34. J.-P. Savineau, R. Marthan, Cytosolic calcium oscillations in smooth muscle cells. *Phys. Ther.* **15**, 50–55 (2000).
35. J. Sneyd, J. M. Han, L. Wang, J. Chen, X. Yang, A. Tanimura, M. J. Sanderson, V. Kirk, D. I. Yule, On the dynamical structure of calcium oscillations. *Proc. Natl. Acad. Sci. U.S.A.* **114**, 1456–1461 (2017).
36. G. D. Frank, S. Eguchi, T. Yamakawa, S.-i. Tanaka, T. Inagami, E. D. Motley, Involvement of reactive oxygen species in the activation of tyrosine kinase and extracellular signal-regulated kinase by angiotensin II*. *Endocrinology* **141**, 3120–3126 (2000).
37. M. Ushio-Fukai, Vascular signaling through G protein-coupled receptors: New concepts. *Curr. Opin. Nephrol. Hypertens.* **18**, 153–159 (2009).
38. L. W. Riedy, R. Chintam, J. S. Walter, Use of a neuromuscular stimulator to increase anal sphincter pressure. *Spinal Cord* **38**, 724–727 (2000).
39. Y. Mandel, R. Manivanh, R. Dalal, P. Huie, J. Wang, M. Brinton, D. Palanker, Vasoconstriction by electrical stimulation: New approach to control of non-compressible hemorrhage. *Sci. Rep.* **3**, 2111 (2013).
40. E. Artimovich, R. K. Jackson, M. B. C. Kilander, Y.-C. Lin, M. W. Nestor, PeakCaller: An automated graphical interface for the quantification of intracellular calcium obtained by high-content screening. *BMC Neurosci.* **18**, 72 (2017).

Acknowledgments: We thank K. Watters for editing of the manuscript. V.N. acknowledges scientific discussions with F. Santoro, M. Cifra, E. D. Glowacki, and N. Apollo. V.N. thanks A. T. Veetil and J. M. Morgan for their comments on the manuscript. **Funding:** This work is supported by the U.S. NIH (NIH NS101488), U.S. Air Force Office of Scientific Research (AFOSR FA9550-18-1-0503), U.S. Army Research Office (W911NF-18-1-0042), and U.S. Office of Naval Research (ONR YIP, N000141612530; PECASE, N000141612958). This work made use of the NUCAPT facility and NUANCE Center, supported through the MRSEC program (NSF DMR-1720139) and the SHyNE Resource (NSF ECCS-1542205) at Northwestern University. We acknowledge the MRSEC Shared User Facilities (NSF DMR-1420709), Integrated Light Microscopy Core and FIB-SEM facility, Department of Geophysical Science at the University of Chicago. **Author contributions:** V.N., J. Yi, and B.T. designed the research. V.N. and J. Yi performed the material synthesis, characterization, in vitro experiments, and data analysis. V.N., M.R., L.M., A.P., and B.T. wrote the paper and received comments and edits from all authors. D.I. and D.N.S. conducted the APT experiments. M.R. performed ex vivo heart pacing experiments. F.S. performed the STEM imaging. L.M. assisted with electrochemistry measurements. X.C. performed the XPS measurements. X.G. performed bacterial disinfection experiments. A.P. performed materials optical microscopy. Y.J. and J.Yu. provided technical assistance. C.T.G. assisted with data analysis. B.T. mentored the research. **Competing interests:** The authors declare that they have no competing interests. **Data and materials availability:** All data needed to evaluate the conclusions in the paper are present in the paper and/or the Supplementary Materials. Additional data related to this paper can be requested from the authors.

Submitted 27 August 2019
Accepted 8 July 2020
Published 21 August 2020
10.1126/sciadv.aaz2743

Citation: V. Nair, J. Yi, D. Isheim, M. Rotenberg, L. Meng, F. Shi, X. Chen, X. Gao, A. Prominski, Y. Jiang, J. Yue, C. T. Gallagher, D. N. Seidman, B. Tian, Laser writing of nitrogen-doped silicon carbide for biological modulation. *Sci. Adv.* **6**, eaaz2743 (2020).